Interstitial hydrogen anions: a cause of *p*-type conductivity in $CsSnI_3$

Yuhang Liang,[1,2] *Xiangyuan Cui*,[3,*] *Feng Li*,[2] *Catherine Stampfl*,[2] *Simon P. Ringer*,[3] *Jun Huang*,[1,*] *Rongkun Zheng*[2,*]

[1] School of Chemical and Biomolecular Engineering, The University of Sydney, NSW 2006, Australia

[2] School of Physics, The University of Sydney, NSW 2006, Australia

[3] School of Aerospace, Mechanical and Mechatronic Engineering, The University of Sydney, NSW 2006, Australia

*Xiangyuan Cui: carl.cui@sydney.edu.au

*Jun Huang: jun.huang@sydney.edu.au

*Rongkun Zheng: rongkun.zheng@sydney.edu.au

Abstract

All-inorganic tin halide perovskite $CsSnI_3$, currently under intensive investigation for photovoltaics and other optoelectronics, characteristically exhibits strong *p*-type conductivity and consequently poor power convention efficiency regardless of growth and processing conditions. This has been traditionally attributed to the prevalence of native acceptor defects; however such a mechanism falls short of explaining the observed high hole concentration under Sn-rich growth conditions in experiments. Here, by using first-principles calculations, we reveal that hydrogen impurities, existing as hydrogen anions, are an important cause for the high *p*-type character in $CsSnI_3$. Hydrogen anions can be present with high densities and act as shallow acceptors, significantly enhancing the background hole concentrations, even under excess Sn treatment. Careful control and utilization of hydrogen anions are important for improving the performance of $CsSnI_3$-based optoelectronic devices.

Keywords: perovskite solar cell, $CsSnI_3$, *p*-type doping, hydrogen, first-principles calculations

Introduction

Organic-inorganic hybrid lead (Pb) halide perovskites have emerged as star materials for next-generation solar cells due to their extraordinary optoelectronic properties, facile fabrication, and low costs[1–3]. The state-of-the-art power conversion efficiency (PCE) has reached up to 25.8% with the potential for challenging the mature silicon-based solar cell market[4]. Nevertheless, the toxicity of the Pb element poses a serious barrier to mass production and commercialization[5]. As one of the leading alternatives within the Pb-free perovskite family, all-inorganic black orthorhombic cesium tin triiodide (B-γ $CsSnI_3$) possesses native inorganic structural stability, a suitable direct bandgap (1.3 eV) for solar cells according to Shockley-Queisser limitation[6], and outstanding optoelectronic properties including a high optical absorption coefficient and low exciton binding energy[7].

Counterintuitively, $CsSnI_3$-based perovskite solar cells suffer seriously from poor device performance thus far with a limited PCE of around 10.8%[8]. Such low PCEs could be intimately associated with a strong *p*-type electrical conductivity[9]. Experimentally, $CsSnI_3$ typically exhibits extremely high background hole concentrations up to $10^{19} - 10^{20} cm^{-3}$ even when nominally undoped[10–12]. Such an unintentional heavy *p*-type character significantly reduces the mobility and lifetime of minority carriers, i.e., electrons, and hence suppresses the photovoltaic device performance. Furthermore, it can also impact other device-related applications, e.g., unbalanced charge injection in light-emitting diodes[13] and a large threshold voltage in field-effect transistors[7,14]. The addition of excess SnX_2 (X = F, Cl, Br, and I) in the precursor solution, namely the Sn-rich growth condition, was reported to mitigate the hole concentration, aiming to enhance the performance of $CsSnI_3$-based photovoltaics[15]. However, such an approach has failed to completely address the issue; notably, the optimized perovskite active layers still exhibit the unipolar *p*-type character with a considerably high hole concentration of $10^{16} - 10^{17} \mathrm{cm}^{-3}$[10–12].

The microscopic origin of this unipolar electrical conductivity in various forms of $CsSnI_3$ has been widely debated. According to the previous reports, it has been commonly speculated being induced by the prevalence of the native defects, in particular, the easy formation of Sn vacancies (V_{Sn}) due to facile oxidation of Sn^{2+}[10,16]. First-principles investigations[17] revealed that $CsSnI_3$ is indeed *p*-type under Sn-poor

growth conditions due to the much lower formation energies of V_{Sn} and Cs vacancies (V_{Cs}) acceptors than those of all donor defects. However, under Sn-rich growth conditions, the contribution of charge compensation from native defects in the $CsSnI_3$ samples would result in a weak *n*-type conductivity, which is contradictory to the experimentally observed strong *p*-type character even with excess Sn treatment[10–12]. A reasonable speculation is that, in addition to the native defects, unintentionally incorporated impurities could play an important role in the *p*-type electrical transport in $CsSnI_3$.

It is well-acknowledged that hydrogen is a common impurity in the lattice of various semiconductors[18–20], which often plays an intricate role in affecting the material properties due to its high mobility and strong chemical activity[19]. Recent studies also showed that hydrogen defect can be present in lead halide perovskite lattices and thus affect the related device performance[21–27], owing to its ubiquity during the growth and processing of these materials[28]. Herein, by performing first-principles hybrid density functional theory calculations, we show that hydrogen anions are energetically stable and can occur as the shallow acceptors with high densities in $CsSnI_3$, and they can play an important role in enhancing the hole concentration and consequently the strong *p*-type character of the material, especially under Sn-rich conditions. These findings clarify the experimental observation of unipolar high *p*-type conductivity even upon excess Sn salt addition to eliminate native acceptors, and shed light on the control and utilization of hydrogen impurities in $CsSnI_3$-based devices.

Computational Method

The first-principles calculations were carried out based on density functional theory (DFT) with the pseudopotential plane-wave (PAW) method as implemented in the Vienna Ab initio Simulation Package (VASP)[29]. The Heyd–Scuseria–Ernzerhof (HSE06) functional[30] ($\alpha = 0.41$) with the consideration of spin-orbit coupling (SOC) was employed with a kinetic energy cutoff of 400 eV. A $2 \times 2 \times 2$ Monkhorst–Pack k-point grid in the Brillouin zone was used for a $2 \times 2 \times 1$ 80-atom supercell based on the orthorhombic $CsSnI_3$ perovskite. The Tkatchenko−Scheffler (TS) correction was adopted to describe the dispersion interactions[31]. The structures were fully relaxed until

the force on each atom was smaller than 0.01 eV/Å. The calculation gives a bandgap value of 1.29 eV, in agreement with the experimental value of 1.30 eV[6]. The relaxed lattice parameters are 8.75, 12.43, and 8.71 Å, respectively, compared with the experimental values of 8.69, 12.38, and 8.64 Å[6]. The defect formation energies were calculated by equations below[32]:

$$\Delta H^f\left(\mathrm{D_i^q}\right) = E\left(\mathrm{D_i^q}\right) - E(host) - \sum n_i(\mu_i + \Delta\mu_i) + q(E_F + E(VBM) + \Delta V) + \Delta_{corr}^{q} \quad (1)$$

here $E\left(\mathrm{D_i^q}\right)$ and $E(host)$ stand for ground-state total energies of the supercells with and without defect, respectively. n_i represents the number of defects added into the supercell. μ_i and $\Delta\mu_i$ are absolute and relative value of the chemical potential. For the chemical potential of hydrogen, it has been commonly used the half of the total energy of an isolated H_2 molecule in previous relevant studies[18], namely the H-rich conditions. To be more practically relevant, we further considered that of various possible H sources including gas H_2O, liquid DMF (C_3H_7NO), acetone (C_3H_6O), ethanol (C_2H_5OH), GBL (γ-butyrolactone), HI, HBr, and solid spiro-OMeTAD, P3HT (Poly(3-hexylthiophene)), FAI ($CH(NH_2)_2I$), n-BA (n-$C_4H_9NH_2$). The liquid-phase structures were obtained by melting the crystalline structure via *ab initio* molecular dynamics (AIMD) using the Nose–Hoover thermostat[33] with the temperatures chosen above the melting points and below the boiling points of the respective liquids, specifically, 300 K for DMF, acetone, ethanol, and GBL, 230 K for HI, and 190 K for HBr. E_F is the Fermi level referenced to the valance band maximum (VBM) and $E(VBM)$ represents the energy of the VBM. ΔV is the correction term for ensuring the alignment of the potential for the charged defect in supercells, and Δ_{corr}^{q} stands for the finite-size correction term for the periodic images of the charged defects[34]. For the most relevant $\mathrm{H_i^-}$, a convergence test using a $3 \times 2 \times 2$ 240-atom supercell of $CsSnI_3$ showed that the calculated formation energy difference between the $2 \times 2 \times 1$ 80-atom and $3 \times 2 \times 2$ 240-atom supercells is only 0.04 eV.

When the orthorhombic-phase $CsSnI_3$ is stable against the formation of the competing secondary compounds of SnI_2, SnI_4, CsI, and Cs_2SnI_6, the relative chemical potential of the elements should satisfy the conditions:

$$\Delta\mu_{Cs} + \Delta\mu_{Sn} + 3\Delta\mu_I = \Delta H_f(CsSnI_3)$$

$$\Delta\mu_{Sn} + 2\Delta\mu_I < \Delta H_f(SnI_2)$$

$$\Delta\mu_{Sn} + 4\Delta\mu_I < \Delta H_f(SnI_4)$$

$$\Delta\mu_{Cs} + \Delta\mu_I < \Delta H_f(CsI)$$

$$2\Delta\mu_{Cs} + \Delta\mu_{Sn} + 6\Delta\mu_I < \Delta H_f(Cs_2SnI_6)$$

where $\Delta H_f(CsSnI_3)$, $\Delta H_f(SnI_2)$, $\Delta H_f(SnI_4)$, $\Delta H_f(CsI)$, and $\Delta H_f(Cs_2SnI_6)$ are the formation enthalpies of $CsSnI_3$, SnI_2, SnI_4, CsI, and Cs_2SnI_6, respectively. Moreover, to avoid the leftover of elemental solids, all the chemical potentials should be less than zero ($\Delta\mu_{Cs} < 0$, $\Delta\mu_{Sn} < 0$, and $\Delta\mu_I < 0$).

The kinetic barriers were calculated based on the nudged elastic band (NEB) method in conjunction with the climbing image method[35], as implemented using the VASP Transition State Tool (VTST), which enables the determination of the minimum energy path between two energetically stable endpoints.

Results and Discussion

For each charged state of atomic hydrogen interstitial H_i, we performed a multiple configuration investigation to determine the most stable defect site in the perovskite lattice. Hydrogen was placed in many positions in the lattice, including $Sn-I$ bond-centered sites, cations (anions) antibonding sites, interstitial void sites, etc., and these defect configurations were fully relaxed. As shown in **Figure 1a**, the positively charged state, namely H_i^+, prefers to reside midway between the two nearby I anions. H_i^+ causes two I^- anions to move closer and hence bridges two iodide sites. The lengths of the two $I-H$ bonds are 1.91 Å and 1.94 Å, respectively. Instead, the neutral-state H_i^0 and negatively charged H_i^- exhibit almost the same local atomic configurations by occupying the positions with the Sn cation as the nearest neighbor. With the presence of H_i^0 or H_i^-, the Sn cation is highly distorted by moving toward the nearby Cs cation from the original host site, reducing the $Cs-Sn$ distance to 4.48 Å for H_i^- or 4.61 Å for H_i^0, as compared with the corresponding value of 5.37 Å in pure $CsSnI_3$. Notably, the Sn-H bond for H_i^- exhibits a similar bond length of ~1.53 Å as that in the hybrid $MASnI_3$ perovskite counterpart (~1.51 Å)[24], while H_i^+, the I-H bond length of ~1.91 Å is much shorter than that of I-H in $MASnI_3$ (~1.42 Å), implying smaller bond strength

of H_i^+ in $CsSnI_3$. This can contribute to the higher formation energy of H_i^+ in $CsSnI_3$.

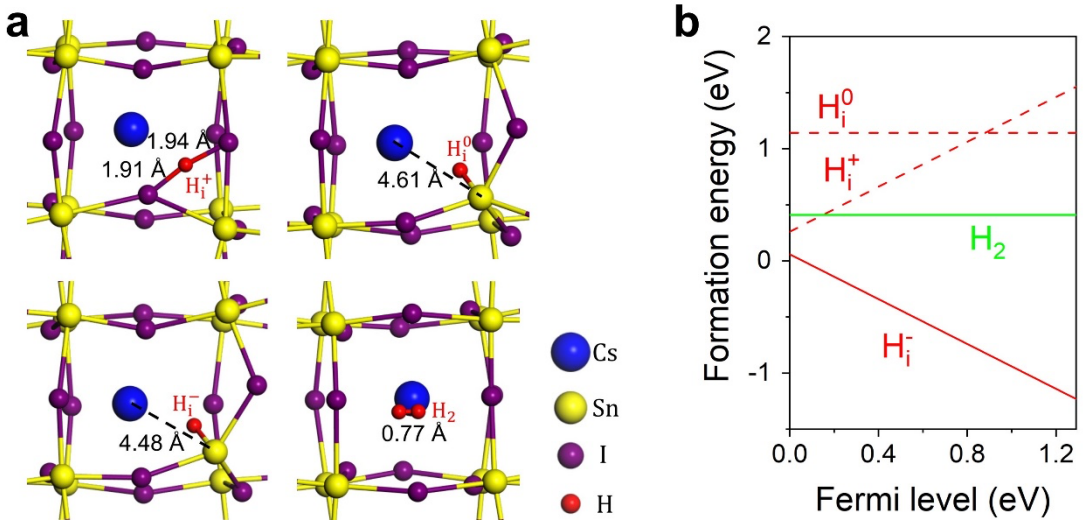

Figure 1. (a) Optimized local atomic structures of H_i^+, H_i^0, H_i^-, and H_2 in $CsSnI_3$. (b) The calculated defect formation energies of interstitial hydrogen defects in $CsSnI_3$ as a function of the Fermi energy (E_F) under the hydrogen-rich conditions.

To qualitatively assess the thermodynamic stability of interstitial hydrogen species in the $CsSnI_3$ perovskite lattice, the calculated formation energies of H_i in three charged states (+, 0, and –) in $CsSnI_3$ as a function of Fermi level E_f under the hydrogen-rich conditions are shown in **Figure 1b**. Importantly, the negatively charged H_i^- is lower in formation energy than H_i^+ and H_i^0 over the whole range of the Fermi level within the bandgap. This behavior is in stark contrast to the cases of many traditional semiconductors (including Si, GaAs, ZnSe, and GaN)[18,19] as well as the hybrid halide perovskite counterparts ($MAPbI_3$ and $MASnI_3$)[22,24], where hydrogen can act as an electric-amphoteric impurity; that is, hydrogen behaves as a donor (H_i^+) in *p*-type material and as an acceptor (H_i^-) in *n*-type one[18], hence often counteracts the prevailing conductivity of the materials. This is the characteristic of the so-called negative-U system with a transition energy level of $\varepsilon(+/-)$ sitting within the bandgap. In comparison, the position of $\varepsilon(+/-)$ of hydrogen is ~0.12 eV below the valance band maximum (VBM) in $CsSnI_3$. Notably, the effect of structural dynamics, which was ignored in the current defect formation energy calculation, may play a role in affecting

the defect stability and the practical transition level[36,37]. The static results show that only ionized hydrogen anion is energetically favorable and hence exclusively serves as a shallow acceptor, behaving as a source of *p*-type conductivity in $CsSnI_3$.

Hydrogen molecules (H_2) is also a common form of hydrogen present in the lattices of solids[19,38]. In contrast to the chemically active H_i, H_2 is stable in the neutral state and prefers a location in the interstitial void, specifically, staying at the center of the $Sn-I$ square plane in $CsSnI_3$. The distance between either hydrogen of the H_2 molecule and the nearest host atom is more than 3 Å, minimizing the interaction with surrounding atoms. The bond length of H_2 is 0.77 Å, slightly longer than that of a free hydrogen molecule, i.e., 0.75 Å. Notably, over the whole range of the Fermi level, H_2 has higher formation energy compared to H_i^-, thus H_2 is precited to play an insignificant role in $CsSnI_3$.

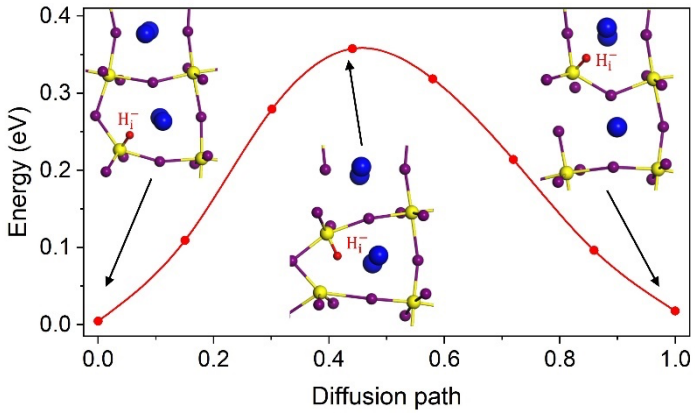

Figure 2. Energy evolution along the energetically most favorable diffusion paths of H_i^- in $CsSnI_3$, where the starting point (x = 0) stands for the initial state and the ending point (x = 1) represents the final state of the diffusion. The highest point corresponds to the transition state. The insets show the local structures of the NEB images at the initial, transition, and final states

We then examined the kinetic properties of H_i^- in $CsSnI_3$. We systematically studied different possible diffusion pathways for H_i^-, and the energy profiles along the minimum energy diffusion path is shown in **Figure 2**. Given the ground state bonding

environment, H_i^- tends to hop from the site originally attached Pb cation to the equivalent adjacent Pb site. Notably, the lattice undergoes a slight structural relaxation in the transition state. The puckered Pb−I−Pb framework pushes hydrogen hopping forward and finally attaching to the targeted Pb site with the structural recovery. The calculated diffusion barrier is 0.37 eV. Significantly, such a barrier value is much lower than that for H_i^- in the hybrid perovskites (e.g., 0.87 eV for $MAPbI_3$ and 0.88 eV for $MASnI_3$)[24], which can be partially attributed to the smaller ionic size of Cs^+ (ionic radius ~1.8 Å) than that of MA organic cation (~2.7 Å)[39], leading to a larger space for H_i^- to move between two interstitial sites. On the other hand, it compares well to the diffusion barrier of the highly mobile iodide vacancy in $MAPbI_3$, i.e., 0.32 eV, which is known to be an important cause of the fast ion diffusion phenomenon[40]. Moreover, hydrogen interstitials could also undertake athermally ionization-enhanced migration, namely the Bourgoin–Corbett mechanism[41], due to the different position preference to the charge state. This mechanism can further faciliate the diffusion of hydrogen interstitial in the lattice of $CsSnI_3$. Based on the low formation energy together with the low kinetic barrier, we predict that H_i^- can be incorporated into the $CsSnI_3$ perovskite lattice with a high density over time upon hydrogen exposure. Significantly, the redistribution of the mobile H_i^- ions under external bias and light illumination is expected to contribute to various irreproducible and unstable properties, most notably the anomalous hysteretic current-voltage (I-V) characteristic of the $CsSnI_3$-based solar cells and other optoelectronic devices[42].

To correlate our results with the experimentally observed electrical character of $CsSnI_3$ under different growth conditions, we first determined the boundaries of the chemical potential of $CsSnI_3$ against its decomposition into the common competing phases (including SnI_2, SnI_4, CsI, and Cs_2SnI_6) as a function of the relative chemical potentials of I and Sn (i.e., $\Delta\mu_I$ and $\Delta\mu_{Sn}$), as shown in **Figure 3a**. There are two representative sets of chemical potentials marked by blue points within the thermodynamically stable range of $CsSnI_3$ (shaded in red), corresponding to the Sn-rich and Sn-poor conditions, respectively. Using the representative chemical potentials, we further examined the stabilities of the native defects. **Figure 3b** shows the calculated formation energies of the five energetically most favorable native defects as well as H_i^- in $CsSnI_3$ under both Sn-rich and Sn-poor conditions. These native defects are the three types of vacancies (V_I, V_{Sn}, and V_{Cs}), an interstitial defect (Sn_i) and an antisite defect (Sn_I). The results are

qualitatively similar to the previous results using a semi-local functional[17] with the difference occurring for the transition levels of Sn_i.

In principle, the electrical conductivity of a material is determined by the formation and compensation between the dominant donors and acceptors. Hence, as shown in **Figure 3b**, the position of E_F can be pinned approximately at the crossing point between the formation energy lines of these two types of the lowest-energy defects. An important feature here is that the formation energy of H_i is substantially low, indicating that hydrogen anions can play an important role in affecting the E_F in $CsSnI_3$. In particular, under the Sn-rich growth conditions, without external impurity incorporation, $CsSnI_3$ should behave as an intrinsic (low-conductivity) semiconductor owing to the full charge compensation among the lowest-energy V_I donors and V_{Cs} acceptors, with the E_F being pinned at the middle of the bandgap (namely, VBM + 0.63 eV). Significantly, with hydrogen being incorporated into the material, the E_F can be shifted toward the VBM and be even pinned at VBM + 0.16 eV by V_I and H_I under the H-rich conditions, resulting in a good *p*-type conductivity. In comparison, under the Sn-poor growth conditions, in agreement with Ref.[17], the robust native acceptors (V_{Sn} and V_{Cs}) lead to a very high hole concentration inherent in $CsSnI_3$. The pinned E_F by V_{Sn} and V_I crosses the edge of the valence band (VBM – 0.02 eV). Moreover, our results show that the presence of H_i can further contribute to the hole concentration and play an increasingly important role, as the E_F can be shifted deeper inside the valence band (VBM – 0.08 eV) pinned by V_I and H_i under the H-rich conditions. Interestingly, the high level hole doping and low E_F below VBM result in degenerate *p*-type semiconductors with essentially metallic properties of $CsSnI_3$, as found in experiments[6].

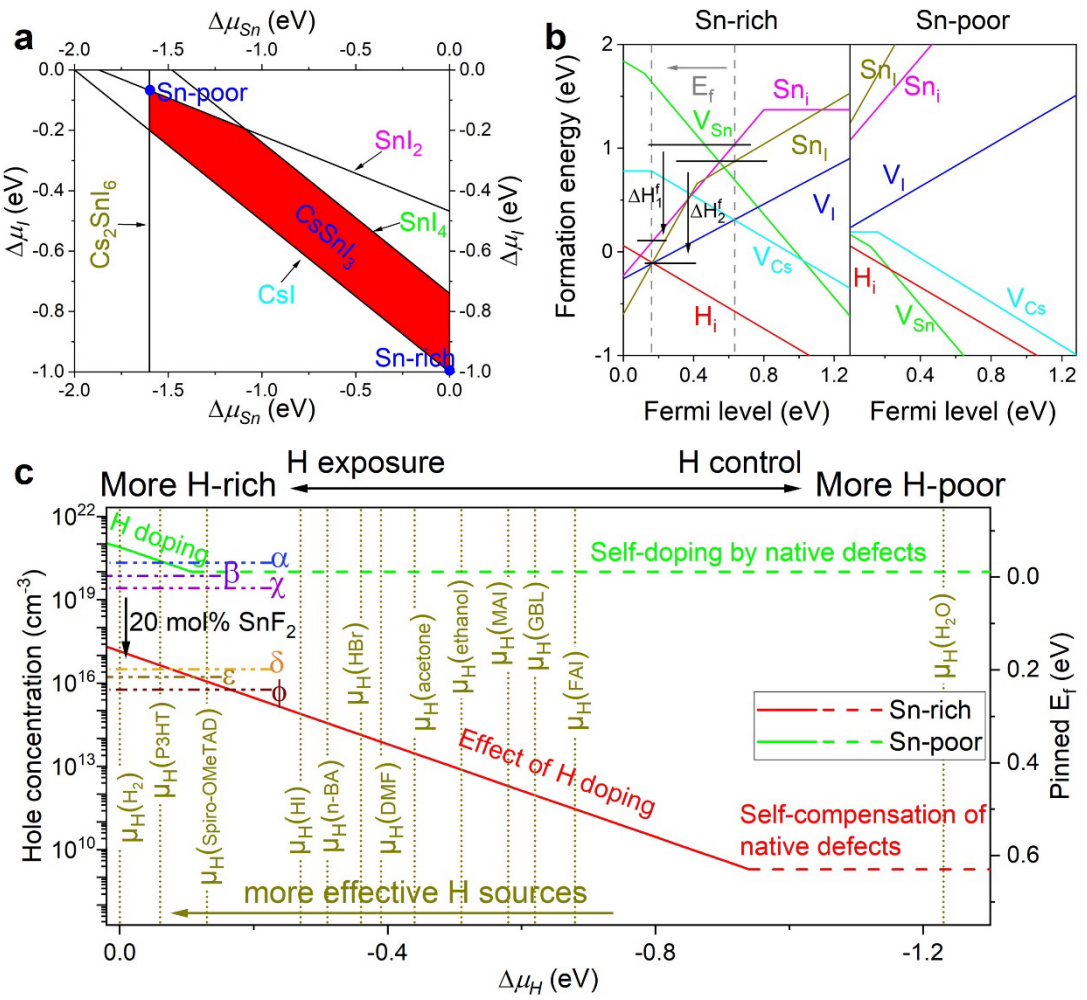

Figure 3. (a) Thermodynamic stability diagram of $CsSnI_3$ against its competing phases as a function of the relative chemical potentials of I ($\Delta\mu_I$) and Sn ($\Delta\mu_{Sn}$). The red-shaded area shows the region where $CsSnI_3$ is thermodynamically stable. (b) The calculated defect formation energies of the five energetically most favorable native defects (V_I, V_{Sn}, V_{Cs}, Sn_i, and Sn_I) as well as the hydrogen anion (under the H-rich conditions) as a function of the Fermi level (E_F) under two representative conditions (the blue points marked by Sn-rich and Sn-poor in (a)). Under Sn-rich conditions, the presence of hydrogen anions shifts the pinned E_F from 0.63 eV to 0.16 eV, correspondingly the conductivity from intrinsic to *p*-type, as marked by the dashed lines. (c) The calculated hole concentration (left Y-axis) and the pinned Fermi level (right Y-axis, referenced to the VBM) as a function of the relative hydrogen chemical potential ($\Delta\mu_H$) of the various possible hydrogen sources, under the Sn-rich conditions (the red line) and Sn-poor conditions (the green line), where the sloped solid-lines stand for the doping effect of hydrogen in $CsSnI_3$, and the horizontal dash-lines stand for the self-compensation or self-doping of the native defects under more H-poor conditions. The

$E_F = 0$ is at the VBM. The experimentally measured hole concentration values of the pristine samples (α from Ref.[10], β from Ref.[9], χ Ref.[12]) and that under Sn-rich growth conditions (δ from Ref.[43], ε from Ref.[10], ϕ from Ref.[12]) were collected for comparison.

To further quantitively and explicitly assess the effect of practical H doping in $CsSnI_3$ practical, we studied the hole concentration (N_h) of the material under the different possible hydrogen conditions. The hole concentration under thermal equilibrium conditions can be estimated as[44]: $N_h = N_V \exp\left(-\frac{E_F - E_V}{k_B T}\right)$, where E_V and E_F are the energies of the VBM and Fermi level, respectively. k_B is the Boltzmann constant and T is the temperature. N_V stands for the effective density of states in the valence band, namely $N_V = 2\left(\frac{2\pi m_h^* k_B T}{h^2}\right)^{\frac{3}{2}}$. Taken from Ref.[45], the effective mass of the hole is $m_h^* = 0.12 m_0$ for B-γ $CsSnI_3$. **Figure 3c** shows the calculated hole concentration as a function of the relative hydrogen chemical potential ($\Delta\mu_H$) under two representative growth conditions of Sn-rich (the red line) and Sn-poor (the green line) in $CsSnI_3$. The right Y-axis stands for the relevant position of the pinned Fermi level referenced to the VBM. Various practically possible H sources were explored for $\Delta\mu_H$. As can be seen, besides H_2 gas of dopant, the dehydrogenation of the organic spiro-OMeTAD and P3HT, which are known as the popular and excellent hole-transporting electron-blocking materials in the perovskite solar cells and other related devices[46], can act as an important origin of unintentional hydrogen contamination in the $CsSnI_3$ layers. In addition, the commonly used HI and HBr additives, and organic solvents such as DMF, acetone, and ethanol, are expected to be the potential H sources during the preparation, indicative of the high probability of hydrogen in $CsSnI_3$.

Note that under the Sn-rich and H-rich conditions, with the effect of H doping, the calculated hole concentration in the $CsSnI_3$ layers can be up to $N_h > 10^{16}$ cm^{-3} at room temperature, in comparison to the value of $\sim 10^9$ cm^{-3} for that under more H-poor conditions due to the full charge compensation of the native defects. In the present case, the shift of H chemical potential by 0.5 eV can enhance the equilibrium density of H by around five orders of magnitude. This can shift the pinned E_F by ~0.25 eV toward the CBM. To correlate the calculated results with experiments, we collected the representative experimental hole concentration of the pristine $CsSnI_3$ (α, β, and χ) and

that with excess Sn treatment (δ, ε, and ϕ) from literature. Indeed, experimental studies[10–12,43] have indicated that $CsSnI_3$ with the excess Sn additions remains the robust *p*-type character with doped hole concentrations as high as $10^{16} - 10^{17}\ \mathrm{cm}^{-3}$. Moreover, such *p*-type conditions can promote the formation of deep-level native Sn_i and Sn_I in the samples. The shift of E_F by the hydrogen incorporation will further lower their formation energies ($\Delta H_1^f \sim 0.94$ eV of Sn_i and $\Delta H_2^f \sim 0.86$eV of Sn_I), as shown in **Figure 3b**. At room temperature, such differences in formation energies imply the enhancement of the defect densities by more than ten orders of magnitude, according to the thermal equilibrium equation[32] of $\Delta N = N_0 e^{-\frac{\Delta H_f}{KT}}$. This could result in the recombination of photogenerated electron-hole pairs and thus impact the performance of $CsSnI_3$-based solar cells and other related optoelectronic devices.

In contrast, under the Sn-poor growth conditions, due to self-doping by the high-density intrinsic V_{Sn} and V_{Cs} acceptors, $CsSnI_3$ originally exhibits heavy *p*-type doping as expected with an exceptionally high hole carrier concentration N_h of $\sim 7 \times 10^{19}\mathrm{cm}^{-3}$ at room temperature, as shown by the green dashed line in **Figure 3c**. Intentional H doping or unintentional H incorporation can further enhance the doped hole concentrations that can reach up to $> 10^{20}\mathrm{cm}^{-3}$ under H-rich conditions. This agrees with the experimental measurements of $N_h \sim 10^{19} - 10^{20}\mathrm{cm}^{-3}$ typically for the untreated $CsSnI_3$ layers. Moreover, the results provide a rationale for the experimental fact that adding excess Sn in $CsSnI_3$ can mitigate the background hole carrier concentration[10,12].

$CsSnI_3$ with unintentional hydrogen incorporation can exhibit a predominantly strong *p*-type electrical property regardless of the growth conditions. The considerably high hole doped concentration can significantly reduce the mobility and lifetime of electrons, which hence essentially limits its application as a light-harvesting material. This is in stark contrast to the hybrid lead halide perovskite counterparts, e.g., $MAPbI_3$ and $FAPbI_3$, which exhibit ambipolar properties: *p*-type, intrinsic (low), and *n*-type conductivities can be flexibly tuned by adjusting the growth conditions (e.g., the molar ratio of precursor during the solution preparation) even with the presence of hydrogen[11,22,25]. Among the family of halide perovskites, hybrid lead halide perovskites with low doping levels (intrinsic semiconductors) can work arguably as the most high-efficient active layers for high-performance solar cells. To mitigate this detrimental

effect, besides an Sn-rich growth condition to reduce the density of the commonly believed native acceptor defects in $CsSnI_3$, effectively suppressing the unintentional incorporation of hydrogen impurity is critical, which in principle can be controlled by minimizing the direct exposure to the potential hydrogen sources during fabrication and operation. On the other hand, $CsSnI_3$ holds promise for unipolar-transport device applications, e.g., hole transporting layers, where hydrogen doping can further enhance the lifetime and diffusion length of hole carriers.

Conclusion

In summary, through first-principles hybrid density functional theory calculations, we demonstrate that, in contrast to the electrically amphoteric behaviors in the many traditional semiconductors and hybrid perovskites, hydrogen exclusively behaves as a shallow acceptor and plays an important role in the prevailing *p*-type conductivity in $CsSnI_3$. In particular, under Sn-rich growth conditions, the presence of hydrogen anions would push the Fermi level towards the VBM and thus significantly enhance the doped hole concentrations, which offers a consistent explanation for the experimental observation of a high background hole carrier concentration and high *p*-type character even after the excess Sn treatment. Furthermore, such *p*-type conditions can further promote the formation of deep-level Sn_i and Sn_I, which are potentially nonradiative recombination centers and hence could impact the optoelectronic properties of $CsSnI_3$. Improving the performance of $CsSnI_3$-based solar cells thus requires both Sn-rich growth conditions and the effective suppression of hydrogen exposure simultaneously. On the other hand, the incorporation of hydrogen could benefit the development of low-cost $CsSnI_3$-based unipolar-transport devices.

Conflict of Interest

The authors declare no conflict of interest.

Acknowledgments

We acknowledge the expert support provided by the Sydney Informatics Hub (SIH) team—a core research facility of the University of Sydney. This work was supported by computational resources provided by the Australian Government through Gadi under the National Computational Merit Allocation Scheme and was accessed through the SIH HPC Allocation Scheme [LE190100021]. We acknowledge partial financial support from the Australian Research Council [DP200100940] and [DE180100167].

Reference

(1) Min, H.; Lee, D. Y.; Kim, J.; Kim, G.; Lee, K. S.; Kim, J.; Paik, M. J.; Kim, Y. K.; Kim, K. S.; Kim, M. G.; Shin, T. J.; Il Seok, S. Perovskite Solar Cells with Atomically Coherent Interlayers on SnO2 Electrodes. *Nature* **2021**, *598* (7881), 444–450. https://doi.org/10.1038/s41586-021-03964-8.

(2) Jeong, J.; Kim, M.; Seo, J.; Lu, H.; Ahlawat, P.; Mishra, A.; Yang, Y.; Hope, M. A.; Eickemeyer, F. T.; Kim, M.; Yoon, Y. J.; Choi, I. W.; Darwich, B. P.; Choi, S. J.; Jo, Y.; Lee, J. H.; Walker, B.; Zakeeruddin, S. M.; Emsley, L.; Rothlisberger, U.; Hagfeldt, A.; Kim, D. S.; Grätzel, M.; Kim, J. Y. Pseudo-Halide Anion Engineering for α-FAPbI 3 Perovskite Solar Cells. *Nature* **2021**, *592* (7854), 381–385. https://doi.org/10.1038/s41586-021-03406-5.

(3) Kim, G.; Min, H.; Lee, K. S.; Lee, D. Y.; Yoon, S. M.; Seok, S. I. Impact of Strain Relaxation on Performance of α-Formamidinium Lead Iodide Perovskite Solar Cells. *Science* **2020**, *370* (6512), 108–112. https://doi.org/10.1126/science.abc4417.

(4) *Best Research-Cell Efficiency Chart*. The efficiency chart published by the National Renewable Energy Laboratory. www.nrel.gov/pv/assets/pdfs/best-research-cell-efficiencies-rev220126.pdf (accessed 2022-01-26).

(5) Ju, M.-G.; Chen, M.; Zhou, Y.; Dai, J.; Ma, L.; Padture, N. P.; Zeng, X. C. Toward Eco-Friendly and Stable Perovskite Materials for Photovoltaics. *Joule* **2018**, *2* (7), 1231–1241. https://doi.org/10.1016/j.joule.2018.04.026.

(6) Chung, I.; Song, J.-H.; Im, J.; Androulakis, J.; Malliakas, C. D.; Li, H.; Freeman, A. J.; Kenney, J. T.; Kanatzidis, M. G. $CsSnI_3$: Semiconductor or Metal? High Electrical Conductivity and Strong Near-Infrared Photoluminescence from a Single Material. High Hole Mobility and Phase-Transitions. *J. Am. Chem. Soc.* **2012**, *134* (20), 8579–8587. https://doi.org/10.1021/ja301539s.

(7) Liang, Y.; Li, F.; Zheng, R. Low-Dimensional Hybrid Perovskites for Field-Effect Transistors with Improved Stability: Progress and Challenges. *Adv. Electron. Mater.* **2020**, *6* (9), 2000137. https://doi.org/10.1002/aelm.202000137.

(8) Ye, T.; Wang, X.; Wang, K.; Ma, S.; Yang, D.; Hou, Y.; Yoon, J.; Wang, K.; Priya, S. Localized Electron Density Engineering for Stabilized B-γ CsSnI3-Based Perovskite Solar Cells with Efficiencies >10%. *ACS Energy Lett.* **2021**, *6* (4), 1480–1489. https://doi.org/10.1021/acsenergylett.1c00342.

(9) Wu, B.; Zhou, Y.; Xing, G.; Xu, Q.; Garces, H. F.; Solanki, A.; Goh, T. W.; Padture, N. P.; Sum, T. C. Long Minority-Carrier Diffusion Length and Low Surface-Recombination Velocity in Inorganic Lead-Free CsSnI3 Perovskite Crystal for Solar Cells. *Advanced Functional Materials* **2017**, *27* (7), 1604818.

https://doi.org/10.1002/adfm.201604818.
(10) Kumar, M. H.; Dharani, S.; Leong, W. L.; Boix, P. P.; Prabhakar, R. R.; Baikie, T.; Shi, C.; Ding, H.; Ramesh, R.; Asta, M.; Graetzel, M.; Mhaisalkar, S. G.; Mathews, N. Lead-Free Halide Perovskite Solar Cells with High Photocurrents Realized Through Vacancy Modulation. *Adv. Mater.* **2014**, *26* (41), 7122–7127. https://doi.org/10.1002/adma.201401991.
(11) Euvrard, J.; Yan, Y.; Mitzi, D. B. Electrical Doping in Halide Perovskites. *Nat Rev Mater* **2021**, *6* (6), 531–549. https://doi.org/10.1038/s41578-021-00286-z.
(12) Matsushima, T.; Hwang, S.; Sandanayaka, A. S. D.; Qin, C.; Terakawa, S.; Fujihara, T.; Yahiro, M.; Adachi, C. Solution-Processed Organic-Inorganic Perovskite Field-Effect Transistors with High Hole Mobilities. *Adv. Mater.* **2016**, *28* (46), 10275–10281. https://doi.org/10.1002/adma.201603126.
(13) Lu, J.; Guan, X.; Li, Y.; Lin, K.; Feng, W.; Zhao, Y.; Yan, C.; Li, M.; Shen, Y.; Qin, X.; Wei, Z. Dendritic CsSnI3 for Efficient and Flexible Near-Infrared Perovskite Light-Emitting Diodes. *Advanced Materials* **2021**, *33* (44), 2104414. https://doi.org/10.1002/adma.202104414.
(14) Liu, A.; Zhu, H.; Bai, S.; Reo, Y.; Zou, T.; Kim, M.-G.; Noh, Y.-Y. High-Performance Inorganic Metal Halide Perovskite Transistors. *Nat Electron* **2022**, *5* (2), 78–83. https://doi.org/10.1038/s41928-022-00712-2.
(15) Heo, J. H.; Kim, J.; Kim, H.; Moon, S. H.; Im, S. H.; Hong, K.-H. Roles of SnX2 (X = F, Cl, Br) Additives in Tin-Based Halide Perovskites toward Highly Efficient and Stable Lead-Free Perovskite Solar Cells. *J. Phys. Chem. Lett.* **2018**, *9* (20), 6024–6031. https://doi.org/10.1021/acs.jpclett.8b02555.
(16) Liang, Y.; Cui, X.; Li, F.; Stampfl, C.; Ringer, S. P.; Zheng, R. First-Principles Investigation of Intrinsic Point Defects in Perovskite ${\mathrm{CsSnBr}}_{3}$. *Phys. Rev. Materials* **2021**, *5* (3), 035405. https://doi.org/10.1103/PhysRevMaterials.5.035405.
(17) Xu, P.; Chen, S.; Xiang, H.-J.; Gong, X.-G.; Wei, S.-H. Influence of Defects and Synthesis Conditions on the Photovoltaic Performance of Perovskite Semiconductor CsSnI $_3$. *Chem. Mater.* **2014**, *26* (20), 6068–6072. https://doi.org/10.1021/cm503122j.
(18) Van de Walle, C. G.; Neugebauer, J. Universal Alignment of Hydrogen Levels in Semiconductors, Insulators and Solutions. *Nature* **2003**, *423* (6940), 626–628. https://doi.org/10.1038/nature01665.
(19) Van de Walle, C. G.; Neugebauer, J. Hydrogen in Semiconductors. *Annu. Rev. Mater. Res.* **2006**, *36* (1), 179–198. https://doi.org/10.1146/annurev.matsci.36.010705.155428.
(20) den Broeder, F. J. A.; van der Molen, S. J.; Kremers, M.; Huiberts, J. N.; Nagengast, D. G.; van Gogh, A. T. M.; Huisman, W. H.; Koeman, N. J.; Dam, B.; Rector, J. H.; Plota, S.; Haaksma, M.; Hanzen, R. M. N.; Jungblut, R. M.; Duine, P. A.; Griessen, R. Visualization of Hydrogen Migration in Solids Using Switchable Mirrors. *Nature* **1998**, *394* (6694), 656–658. https://doi.org/10.1038/29250.
(21) Egger, D. A.; Kronik, L.; Rappe, A. M. Theory of Hydrogen Migration in Organic-Inorganic Halide Perovskites. *Angew. Chem. Int. Ed.* **2015**, *54* (42), 12437–12441. https://doi.org/10.1002/anie.201502544.
(22) Liang, Y.; Cui, X.; Li, F.; Stampfl, C.; Huang, J.; Ringer, S. P.; Zheng, R. Hydrogen-Anion-Induced Carrier Recombination in MAPbI3 Perovskite Solar Cells. *J. Phys. Chem. Lett.* **2021**, *12* (43), 10677–10683. https://doi.org/10.1021/acs.jpclett.1c03061.

(23) Liang, Y.; Cui, X.; Li, F.; Stampfl, C.; Ringer, S. P.; Huang, J.; Zheng, R. Hydrogen-Induced Nonradiative Recombination in All-Inorganic CsPbI3 Perovskite Solar Cells. *Solar RRL n/a* (n/a), 2200211. https://doi.org/10.1002/solr.202200211.
(24) Liang, Y.; Cui, X.; Li, F.; Stampfl, C.; Ringer, S. P.; Zheng, R. Atomic and Molecular Hydrogen Impurities in Hybrid Perovskite Solar Cells. *J. Phys. Chem. C* **2022**, *126* (4), 1721–1728. https://doi.org/10.1021/acs.jpcc.1c10339.
(25) Liang, Y.; Cui, X.; Li, F.; Stampfl, C.; Ringer, S. P.; Huang, J.; Zheng, R. Minimizing and Controlling Hydrogen for Highly Efficient Formamidinium Lead Triiodide Solar Cells. *J. Am. Chem. Soc.* **2022**, *144* (15), 6770–6778. https://doi.org/10.1021/jacs.2c00038.
(26) Zhang, X.; Shen, J.-X.; Turiansky, M. E.; Van de Walle, C. G. Minimizing Hydrogen Vacancies to Enable Highly Efficient Hybrid Perovskites. *Nat. Mater.* **2021**, *20* (7), 971–976. https://doi.org/10.1038/s41563-021-00986-5.
(27) Sadhu, S.; Buffeteau, T.; Sandrez, S.; Hirsch, L.; Bassani, D. M. Observing the Migration of Hydrogen Species in Hybrid Perovskite Materials through D/H Isotope Exchange. *J. Am. Chem. Soc.* **2020**, *142* (23), 10431–10437. https://doi.org/10.1021/jacs.0c02597.
(28) Ceratti, D. R.; Zohar, A.; Kozlov, R.; Dong, H.; Uraltsev, G.; Girshevitz, O.; Pinkas, I.; Avram, L.; Hodes, G.; Cahen, D. Eppur Si Muove: Proton Diffusion in Halide Perovskite Single Crystals. *Adv. Mater.* **2020**, *32* (46), 2002467. https://doi.org/10.1002/adma.202002467.
(29) Kresse, G.; Joubert, D. From Ultrasoft Pseudopotentials to the Projector Augmented-Wave Method. *Phys. Rev. B* **1999**, *59* (3), 1758–1775. https://doi.org/10.1103/PhysRevB.59.1758.
(30) Heyd, J.; Scuseria, G. E.; Ernzerhof, M. Erratum: “Hybrid Functionals Based on a Screened Coulomb Potential” [J. Chem. Phys. 118, 8207 (2003)]. *The Journal of Chemical Physics* **2006**, *124* (21), 219906. https://doi.org/10.1063/1.2204597.
(31) Tkatchenko, A.; Scheffler, M. Accurate Molecular Van Der Waals Interactions from Ground-State Electron Density and Free-Atom Reference Data. *Phys. Rev. Lett.* **2009**, *102* (7), 073005. https://doi.org/10.1103/PhysRevLett.102.073005.
(32) Kang, J.; Li, J.; Wei, S.-H. Atomic-Scale Understanding on the Physics and Control of Intrinsic Point Defects in Lead Halide Perovskites. *Applied Physics Reviews* **2021**, *8* (3), 031302. https://doi.org/10.1063/5.0052402.
(33) Nosé, S. A Unified Formulation of the Constant Temperature Molecular Dynamics Methods. *J. Chem. Phys.* **1984**, *81* (1), 511–519. https://doi.org/10.1063/1.447334.
(34) Freysoldt, C.; Neugebauer, J.; Van de Walle, C. G. Fully Ab Initio Finite-Size Corrections for Charged-Defect Supercell Calculations. *Phys. Rev. Lett.* **2009**, *102* (1), 016402. https://doi.org/10.1103/PhysRevLett.102.016402.
(35) Henkelman, G.; Uberuaga, B. P.; Jónsson, H. A Climbing Image Nudged Elastic Band Method for Finding Saddle Points and Minimum Energy Paths. *The Journal of Chemical Physics* **2000**, *113* (22), 9901–9904. https://doi.org/10.1063/1.1329672.
(36) Cohen, A. V.; Egger, D. A.; Rappe, A. M.; Kronik, L. Breakdown of the Static Picture of Defect Energetics in Halide Perovskites: The Case of the Br Vacancy in CsPbBr3. *J. Phys. Chem. Lett.* **2019**, *10* (16), 4490–4498. https://doi.org/10.1021/acs.jpclett.9b01855.
(37) Chu, W.; Zheng, Q.; Prezhdo, O. V.; Zhao, J.; Saidi, W. A. Low-Frequency Lattice Phonons in Halide Perovskites Explain High Defect Tolerance toward

Electron-Hole Recombination. *Sci. Adv.* **2020**, *6* (7), eaaw7453. https://doi.org/10.1126/sciadv.aaw7453.

(38) Lavrov, E. V.; Herklotz, F.; Weber, J. Identification of Hydrogen Molecules in ZnO. *Phys. Rev. Lett.* **2009**, *102* (18), 185502. https://doi.org/10.1103/PhysRevLett.102.185502.

(39) Saliba, M.; Matsui, T.; Seo, J.-Y.; Domanski, K.; Correa-Baena, J.-P.; Nazeeruddin, M. K.; Zakeeruddin, S. M.; Tress, W.; Abate, A.; Hagfeldt, A.; Grätzel, M. Cesium-Containing Triple Cation Perovskite Solar Cells: Improved Stability, Reproducibility and High Efficiency. *Energy Environ. Sci.* **2016**, *9* (6), 1989–1997. https://doi.org/10.1039/C5EE03874J.

(40) Haruyama, J.; Sodeyama, K.; Han, L.; Tateyama, Y. First-Principles Study of Ion Diffusion in Perovskite Solar Cell Sensitizers. *J. Am. Chem. Soc.* **2015**, *137* (32), 10048–10051. https://doi.org/10.1021/jacs.5b03615.

(41) Bourgoin, J. C.; Corbett, J. W. A New Mechanism for Interstistitial Migration. *Physics Letters A* **1972**, *38* (2), 135–137. https://doi.org/10.1016/0375-9601(72)90523-3.

(42) Ye, T.; Wang, K.; Hou, Y.; Yang, D.; Smith, N.; Magill, B.; Yoon, J.; Mudiyanselage, R. R. H. H.; Khodaparast, G. A.; Wang, K.; Priya, S. Ambient-Air-Stable Lead-Free CsSnI3 Solar Cells with Greater than 7.5% Efficiency. *J. Am. Chem. Soc.* **2021**, *143* (11), 4319–4328. https://doi.org/10.1021/jacs.0c13069.

(43) Sabba, D.; Mulmudi, H. K.; Prabhakar, R. R.; Krishnamoorthy, T.; Baikie, T.; Boix, P. P.; Mhaisalkar, S.; Mathews, N. Impact of Anionic Br^- Substitution on Open Circuit Voltage in Lead Free Perovskite ($CsSnI_{3-x}Br_x$) Solar Cells. *J. Phys. Chem. C* **2015**, *119* (4), 1763–1767. https://doi.org/10.1021/jp5126624.

(44) Semiconductors. In *Physics of Solar Cells*; John Wiley & Sons, Ltd, 2005; p 71. https://doi.org/10.1002/9783527618545.ch3.

(45) Su, Y.; Song, K.-K.; Zhong, M.; Shi, L.-B.; Qian, P. Stability and Phonon-Limited Mobility for CsSnI3 and CsPbI3. *Journal of Alloys and Compounds* **2021**, *889*, 161723. https://doi.org/10.1016/j.jallcom.2021.161723.

(46) Jeong, M.; Choi, I. W.; Go, E. M.; Cho, Y.; Kim, M.; Lee, B.; Jeong, S.; Jo, Y.; Choi, H. W.; Lee, J.; Bae, J.-H.; Kwak, S. K.; Kim, D. S.; Yang, C. Stable Perovskite Solar Cells with Efficiency Exceeding 24.8% and 0.3-V Voltage Loss. *Science* **2020**, *369* (6511), 1615–1620.

TOC Graphic